Design and tests of a portable mini gamma camera

F. Sánchez,[a] J. M. Benlloch, B. Escat, N. Pavón, E. Porras, D. Kadi-Hanifi, and J. A. Ruiz
Instituto de Física Corpuscular (CSIC-UV), Edificio Institutos de Paterna, P.O. Box 22085, E-46071 Valencia, Spain

F. J. Mora and A. Sebastià
Departamento Ingeniería Electrónica, University Politécnica de Valencia, Camí de Vera s/n, Valencia, Spain

(Received 18 December 2003; revised 7 April 2004; accepted for publication 7 April 2004; published 20 May 2004)

Design optimization, manufacturing, and tests, both laboratory and clinical, of a portable gamma camera for medical applications are presented. This camera, based on a continuous scintillation crystal and a position-sensitive photomultiplier tube, has an intrinsic spatial resolution of ≈ 2 mm, an energy resolution of 13% at 140 keV, and linearities of 0.28 mm (absolute) and 0.15 mm (differential), with a useful field of view of 4.6 cm diameter. Our camera can image small organs with high efficiency and so it can address the demand for devices of specific clinical applications like thyroid and sentinel node scintigraphy as well as scintimammography and radio-guided surgery. The main advantages of the gamma camera with respect to those previously reported in the literature are high portability, low cost, and weight (2 kg), with no significant loss of sensitivity and spatial resolution. All the electronic components are packed inside the minigamma camera, and no external electronic devices are required. The camera is only connected through the universal serial bus port to a portable personal computer (PC), where a specific software allows to control both the camera parameters and the measuring process, by displaying on the PC the acquired image on ''real time.'' In this article, we present the camera and describe the procedures that have led us to choose its configuration. Laboratory and clinical tests are presented together with diagnostic capabilities of the gamma camera.
[DOI: 10.1118/1.1755570]

Key words: nuclear medicine, radionuclide imaging, scintillation counting, gamma cameras

I. INTRODUCTION

Since its introduction in 1958, the Anger gamma camera[1] has been continuously developed and has become the standard choice for clinical *in vivo* explorations. It provides space-temporal information about the distribution of a radiotracer administered to a patient allowing noninvasive measurement of physiological functions. In nuclear medicine, the most common imaging systems are general-purpose systems, which allow a wide variety of morphological and physiological studies. While dedicated x-ray equipment for specific examinations are largely found in diagnostic radiology, this is not the case for nuclear medicine, where general purpose gamma cameras are commonly used. However, general purpose gamma cameras when used for imaging a small organ, like the thyroid or the sentinel node, have disadvantages related to their large and awkward size, and relatively high cost per study. For these small organ studies, the large detector of a standard gamma camera cannot in general be brought very close to the organ of interest, thus accepts background activity from other organs and allows only certain views to be taken. These factors imply that the general purpose gamma cameras have non optimized spatial resolution and lower image contrast for imaging small organs. These reasons, together with the high cost per study when using standard nuclear imaging systems, limit their usefulness for small organ studies.

For the earlier reasons, in the past few years there has been an increasing demand for compact gamma cameras with low cost, light weight and small field of view (FOV).[2–4] The small gamma cameras develop imaging tasks requiring specific procedures and provide higher image quality than a general-purpose camera. Such small gamma cameras may be useful for imaging small organs such as thyroid and sentinel node as well as for scintimammography applications[5–9] or radio-guided surgery.[10]

Here we describe a small portable and low cost gamma camera designed and built at our laboratory. The minigamma camera has an overall size of 90 mm diameter and 200 mm length with a total weight of 2 kg. Special emphasis has been put on low cost and high portability. The main components of our camera are a collimator, a continuous scintillation crystal as gamma-ray detector, a position-sensitive photomultiplier tube (PSPMT), signal conforming analog electronics, and a digital processor. We have conducted several studies in order to characterize and optimize these main components, such as the PSPMT and the scintillator. Recently, a great effort has been done in the development of high stopping power, room temperature semiconductor pixelated arrays.[11,12] Even market products based on CdZnTe semiconductor detectors are today available (http://www.korins.com/m/ev/cameraE.htm; Anzai Medical, ''eZ-SCOPE'' gamma camera). Although semiconductor technol-

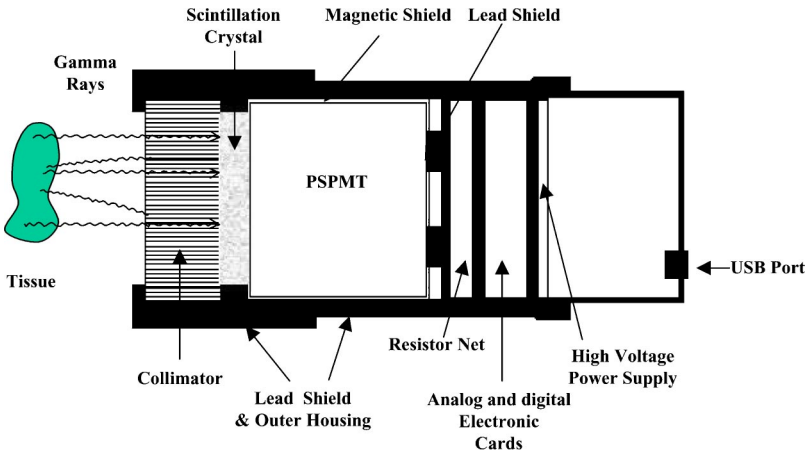

FIG. 1. Schematic of the minigamma camera components. The parallel-hole collimator configuration is showed.

ogy offers high spatial resolution and compactness, it has as main drawback the difficulty to obtain thick crystals at reasonable cost. Besides, such room temperature semiconductor detectors exhibit marked hole trapping effect while many pixels (each one with its own low noise charge sensitive preamplifiers) are required to conform the detector plane. For these reasons, most of the small gamma cameras developed to date have used scintillation detectors.[13] Moreover, these small gamma cameras are mainly based on pixelated scintillation crystal array instead of a conventional monocrystal, coupled to a PSPMT.[7] With this technology based on pixelated crystals, normal values for the intrinsic spatial resolution are about 2 mm. However, crystal pixelation increases the cost and complexity of the camera design. Moreover, in a scintillation pixelated detector, energy resolution is a function not only of the intrinsic scintillation efficiency of the crystals, but also of the crystal size, with smaller cross-section crystals exhibiting greater light loss and, consequently, lower energy resolution. Minigamma cameras based on intensified position sensitive diode instead of photomultiplier tubes have been also recently developed.[14] In these cameras spatial resolution between 1 and 2 mm are achieved together with a high sensitivity, although they exhibit low energy resolution (32% @ 140 keV).

Our camera is based on a continuous crystal. By optimizing the final crystal and PSPMT configuration together with a low noise specific designed electronic circuitry, we achieve an intrinsic spatial resolution of 2 mm, thus reducing cost and complexity, with no significant loss of sensitivity. Our camera is fully portable, which represents another important advantage with respect to those previously reported in the literature.[2,4,15,16] Recently gamma cameras based on the same PSPMT we propose have been described in the literature and commercialized. However, in these cases external electronic CAMAC modules[17] or a specific external control unit are needed (Intramedical Imaging Inc.; http://www.intramedical.com/IMI/mcam.html), thus increasing cost and complexity. All the electronic components, including the ADC and the PSPMT power supply, are packed inside the minigamma camera we propose and no external electronic devices are required. The camera is only connected through the universal serial bus (USB) port to a portable personal computer (PC), and no acquisition card must be plugged into the PC. We have developed a specific data processing software that allows one to control both the camera parameters, including PSPMT high voltage power supply, and the measuring process. The software also displays on the PC the acquired image on ''real time.''

In this article, we present the camera and describe the procedures that have led us to choose its configuration. Laboratory and clinical tests that were carried out are also described together with diagnostic capabilities of the gamma camera, mainly focused on thyroid scintigraphy.

II. CAMERA DESIGN AND OPERATION PRINCIPLES

The design of the portable minigamma camera was optimized for the radioactive source most widely used in medical explorations, ^{99m}Tc, which emits gamma rays of 140 keV. The camera is composed of a single position-sensitive photomultiplier tube (Hamamatsu R2486, Sec. II B) coupled to a continuous scintillation crystal, a lead collimator, and the signal circuitry, including analog and digital signal processing (see Fig. 1). Two different kind of collimators have been considered: parallel-holes and pinhole collimators.

The scintillation crystal is coupled to a PSPMT with optical grease. Electronic cards that have been developed in our laboratory constitute the next stage (Sec. II C). The camera is covered by mu-metal as magnetic shield to avoid shifts in the position signals due to external magnetic fields. The crystal and the PSPMT are surrounded by a lead layer 4-mm-thick for gamma radiation shielding (Fig. 1).

All the earlier elements are fixed inside a cylindrical aluminum case 90 mm in diameter and 200 mm in length with the USB port connector placed at the back face (Fig. 2). Finally, rubber seals between the case pieces produce a light proof environment within the camera head. The small dimensions of the system together with its light weight of 2 kg, ensure easy portability and allows to bring the camera very close to the organ of interest, increasing the sensitivity and spatial resolution.

FIG. 2. The minigamma camera.

A. The scintillator: Optimization and characterization

The gamma camera characteristics greatly depend on the scintillation crystal that is coupled to the PSPMT. The degree of image compression[18] depends on the reflection properties of the crystal edges. Reflective edges (white painted) shift the centroids of photon distributions that are close to the crystal edges towards the center. Black-edge crystals absorb scintillation photons emitted towards the edges and do not contribute to the light output distribution. For this reason, black-edge crystals exhibit lower image compression than white-edge ones. In order to optimize scintillation crystal conditioning, simulations were performed in order to predict linearity and spatial resolution for different crystal surface finishes. The GEANT-3 (R. Brun and F. Carminati, GEANT detector description and simulation tool, CERN Program Library W5013, 1993) and DETECT2000 (C. Moisan, F. Cayouet and G. McDonald, DETECT 2000 User's Guide) packages have been used to determine both the position of absorption in the crystal of 122 keV gammas emitted by a point source and the optical light production and transport to the photocathode, respectively. The energy of 122 keV was assumed in order to compare with laboratory test done with collimated ^{57}Co point sources. The PSPMTs response and the camera collimator were not considered in these simulations. Simulations have been performed for both NaI(Tl) (51 mm diameter and 6 mm thick) and CsI(Na) (51 mm diameter and 4 mm thick). The crystal diameter was chosen to fit the useful photocathode area of the PSPMT. The thickness of the crystal was chosen as a trade-off between the intrinsic spatial resolution and the detection efficiency at 140 keV, since increasing thickness produces a degradation of the spatial resolution. Finally, these thickness assure an intrinsic full peak efficiency of 70% for NaI(Tl) and 67% for CsI(Na) at 140 keV. Up to five different surface finishes were considered for the simulations: white-painted, black-painted, entrance face white-painted and edge black-painted, entrance face black-painted and edge white-painted and, finally, without any painted surface. In the case of NaI(Tl), a 1-mm-thick glass window was considered in the simulation. Results for intrinsic linearity and spatial resolution are shown in Fig. 3. CsI(Na) crystal was found to produce better results than NaI(Tl). This result was independent of the surface finish and is probably due to the fact that it does not need a glass entrance window which always results in light spreading. In both cases, CsI(Na) and NaI(Tl), the best compromise between linearity and spatial resolution was found when crystals are black-painted, although this design would imply a loss of energy resolution.

B. The PSPMT

The PSPMT Hamamatsu R2486 consists of a circular proximity-type photocathode, 12-staged mesh dynodes, and 32 crossed-wire anodes, arranged in two orthogonal groups (X and Y) covering a circular area 60 mm in diameter. The useful photocathode area of the PSPMT is 50 mm in diameter. The anode outputs are connected to a resistive current divider network (Fig. 4) in order to reduce the number of signals that need to be read from 32 to 4 (XA, XB, YC, YD in Fig. 4). The maximum radiant sensitivity and quantum efficiency of its photocathode at $\lambda = 420$ nm matches well the 415–420 nm maximum of the intensity light emitted by the scintillation crystals.

Electrons emitted from the photocathode collide with the dynodes, resulting in a multiplication cascade of secondary electrons. The electron cloud emitted from the last dynode (reflecting type) is collected by the anodes and is distributed in four charges arriving at the resistive divider ends (Q_{XA}, Q_{XB}, Q_{YC}, and Q_{YD}). The centroid position (X,Y) of the incident light pulse distribution on the photocathode can be obtained by Anger's equations,[1] (see Fig. 4). The sum of the four charges provides the total energy deposited by the incident gamma ray.

C. Electronics

A readout circuit capable to integrate and digitize the currents generated at the PSPMT was developed and built at our laboratory.[19] Special care was put during design phase in order to ensure full portability and low electronic noise of the camera. Full portability means that all the electronics must be completely integrated inside the gamma camera, which is connected through the USB port to a portable PC. This requirement implies that the electronic design must assure low electric consumption as the portable PC acts also as the gamma camera power supply. No acquisition card must be plugged into the PC. Low electronic noise is another important design driver, in order to improve the spatial and energy resolutions. A complete description of the gamma camera electronics can be found in Ref. 19, here we only describe the main characteristics of the design. The electronics of the gamma camera (Fig. 5) consists in three electronic cards: the analog card, the digital card, and the power supply card. The analog card integrates the currents generated at the PSPMT with a fall time of 47 μs, which is much bigger than the scintillation light decay time and thus optimizes energy resolution. This analog card also filters, amplifies, and conforms the signals in order to digitize them properly. The digital card includes a 11-bit analog-to-digital converter (ADC) and a microcontroller. Such microcontroller stores

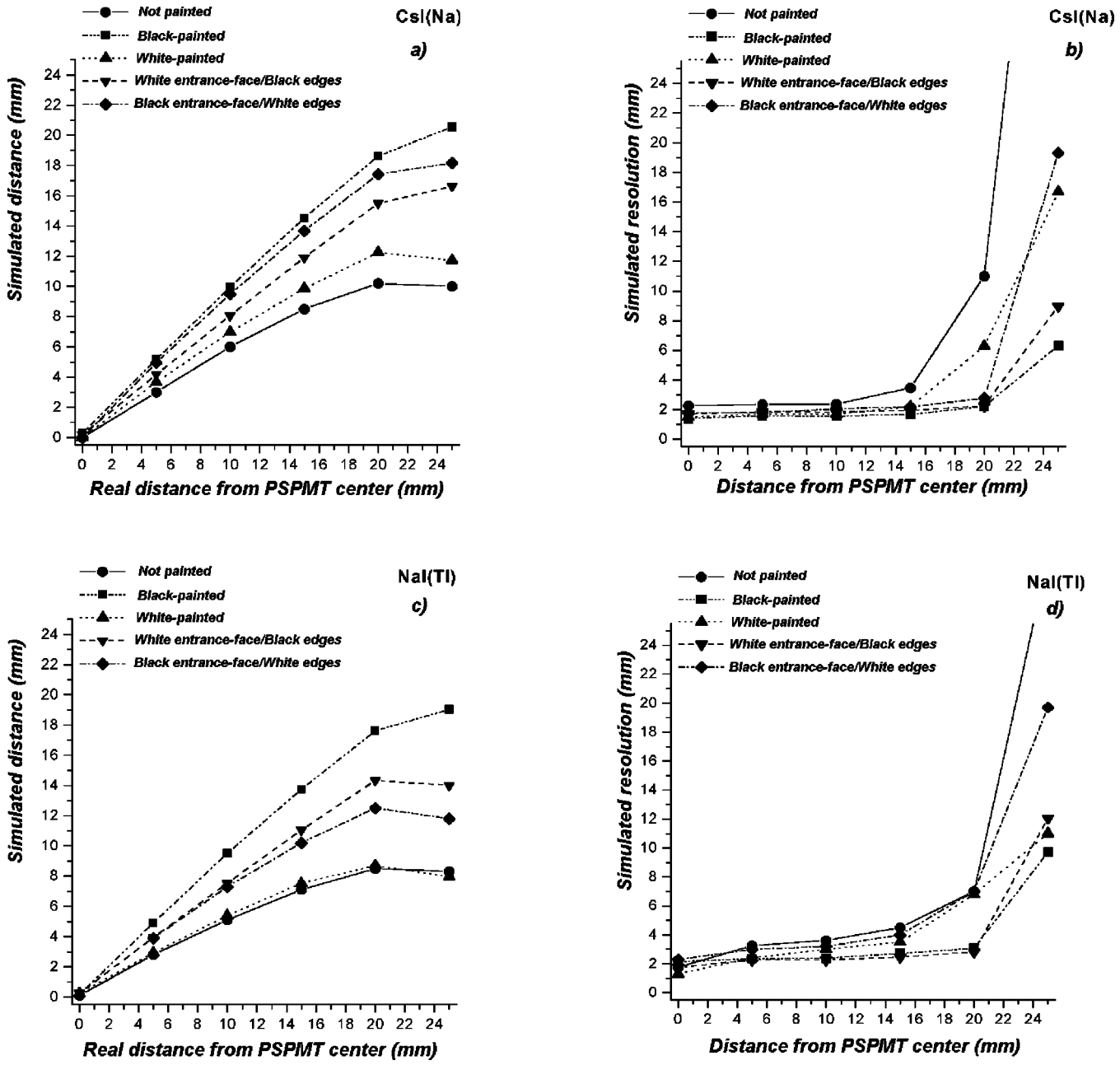

FIG. 3. Intrinsic linearity (a),(c) and spatial resolution (b),(d) obtained by simulation of a CsI(Na) crystal and a NaI(Tl) crystal with different surface finishes.

and sends the digitized data to the PC through the USB port. The microcontroller allows also to choose the energy threshold level for the ADC to digitize the signals. Finally, the power supply card generates all the operating voltages needed by the gamma camera, including the PSPMT high voltage. These voltages are supplied by this card using a single 5 V (500 mA maximum) input through the USB port. This electronic design allows a low noise (signal-to-noise Ratio better than 60 dB), compact, and fully portable gamma camera. An easy to use specific data processing software developed by us allows to control both the camera parameters and the measuring process. The data processing was designed to perform a real time image refresh during examination, after the energy and position of the event are properly computed (Sec. IV A).

III. LABORATORY TEST RESULTS

A. Intrinsic responses of PSPMTs

In general, PSPMTs exhibit marked differences with regard to pulse height uniformity and linearity response, which make necessary to characterize individually the intrinsic response of the PSPMTs used in gamma cameras.

The intrinsic response of two PSPMTs R2486-type (named PSPMT A and B) were measured by illuminating their entrance window with 450 nm blue light emitting diode (LED) pulses. A grid with 2 mm distance between impinging positions (real $X-Y$, Fig. 6) was used. The light from the LED to the PSPMT was driven through a 1 mm diameter optical fiber, whose position was governed by a computer controlled $X-Y$ translation stage. The ''total energy'' of the

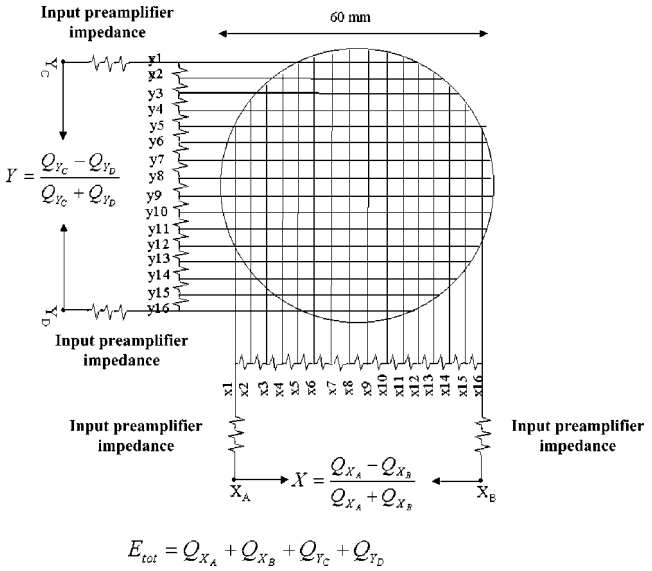

FIG. 4. Crossed-wire anode structure of the PSPMT used in this work. The resistor chain is also shown. $X(Y)1...X(Y)16$ refer to the PSPMT anodes.

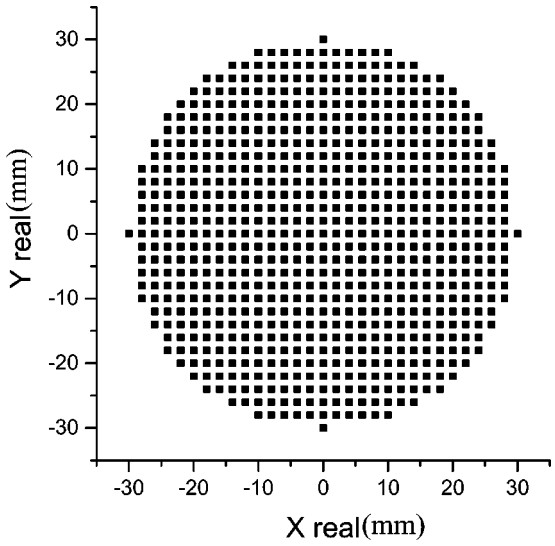

FIG. 6. Impinging positions of blue LED pulses used for intrinsic response determination of PSPMTs.

events and their corresponding positions (measured $X-Y$) were calculated for each source location following Anger's equations. Measurements at two different voltages (-1000 and -1200 V) were taken. The results are shown in Fig. 7. Concerning pulse height uniformity, the PSPMTs exhibit a marked non-uniform response across their sensitive surface areas. Both maps (and particularly that of PSPMT A, Fig. 7) are noticeably asymmetric, this behavior being observed previously.[20] Relative differences between areas of maximum and minimum pulse height values are 66%, 75% (PSPMT A) and 43%, 33% (PSPMT B) at -1000 and -1200 V, respectively. Thus, PSPMT B is more uniform than A and also has a more symmetric response. Photomultipliers A and B also compress images as shown in the distortion maps (Fig. 7). This is due to variations of the electron trajectories caused by differences in the electric field at the dynode surface and especially at their edges. By comparing PSPMTs A and B distortion maps at the same voltage, one can conclude that PSPMT A maps are less distorted than Bs, and also the border points are better distinguished for PSPMT A. Linearity curves (Fig. 7) show the common general shape of a linear response with flattened ends. Although both PSPMTs show a quite similar behavior, the PSPMT A response is more linear with lower dispersion on the measured values. According to these results, we decided to use

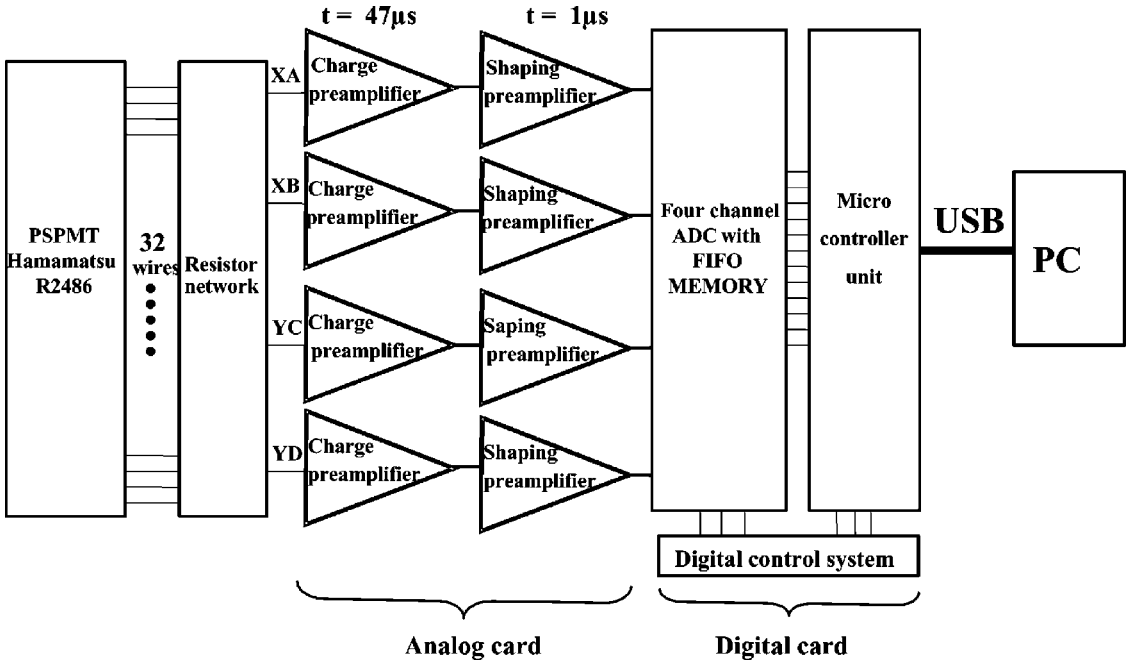

FIG. 5. Electronic chain general scheme.

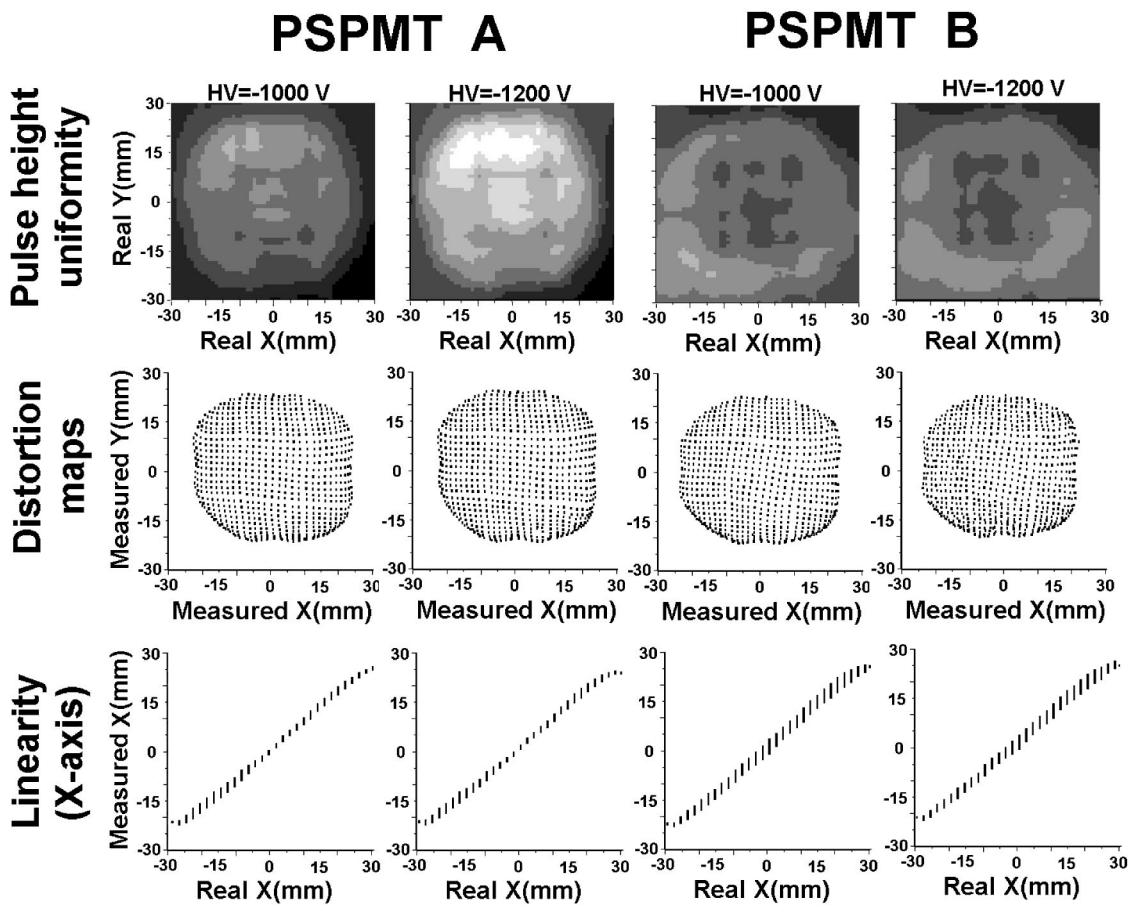

FIG. 7. Results of pulse height uniformity (dark black: maximum value, light gray: minimum value), measured XY positions and linearity of X axis for PSPMTs A and B at $HV=-1000$ and -1200 V.

PSPMT A for the gamma camera characterization and performance determination.

B. Imaging characteristics

Taking into account the results obtained by simulations when considering different scintillation crystals with different surface finishes (Sec. II A), experimental measurements were performed using CsI(Na) and NaI(Tl) crystals with two surface finishes: (1) totally black-painted and (2) white entrance face with black edges (in what follows we call this configuration ''black-white''). The objective is to experimentally determine the optimal configuration for the gamma camera, as simulations showed no significant differences for these configurations. Crystal dimensions were the same assumed for the simulations: NaI(Tl) 6 mm thick and CsI(Na) 4 mm thick, both 51 mm in diameter. In the case of the NaI(Tl), it was sealed by 1-mm-thick glass for optical coupling to the photocathode window. The PSPMT A was used for the measurements. No camera collimator was used in order to obtain the intrinsic values of linearity, spatial resolution, and energy resolution.

A 1 mm diameter collimated ^{57}Co 10 μCi (1 Ci$=3.7\times10^{10}$ Bq) point source was used to perform these measurements. The source was located in 81 different positions equally spaced by 5 mm distance within a circular region of 50 mm diameter centered on the crystal. The images obtained with the four crystals tested can be seen in Fig. 8. Figure 9 shows the experimental intrinsic linearity curves obtained for these crystals. The best linearity response is obtained when crystals are black-painted (absorptive walls reduce the typical position linearity response losses). The CsI(Na) black-painted crystal produces the lower image compression (60% of the image's original size), while the NaI(Tl) black-white painted crystal provides the bigger compression among the tested configurations (40% of the image's original size). Compression makes source points near the crystal edge hardly distinguishable in the raw image, which complicates their later formation.

Figure 10 shows the intrinsic spatial resolution curves obtained from the experimental measurements. CsI(Na) crystals provide the best results independently of the surface finish considered (2 mm on average for points located up to a distance of 20 mm from the center of the field of view). Notice that near the crystal borders there is a worsening in resolution. From Figs. 8 to 10 we can conclude that the useful field of view (UFOV) of the gamma camera is about 46 mm in diameter. The general tendencies experimentally observed regarding linearity and spatial resolution agree with simulations (Fig. 3), although quantitatively, experimental values are worse than those found by simulations. These quantita-

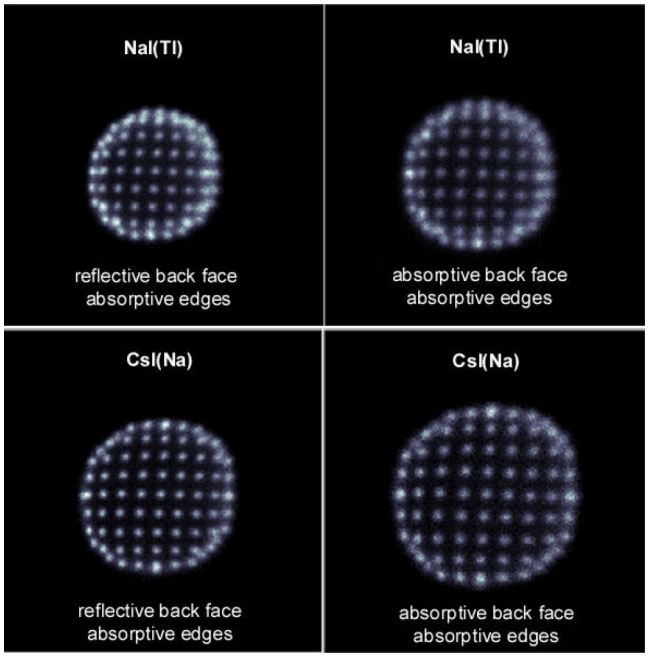

FIG. 8. Images obtained with the four crystals tested. No posterior image treatment has been used, thus the images have been obtained by direct application of Anger equations.

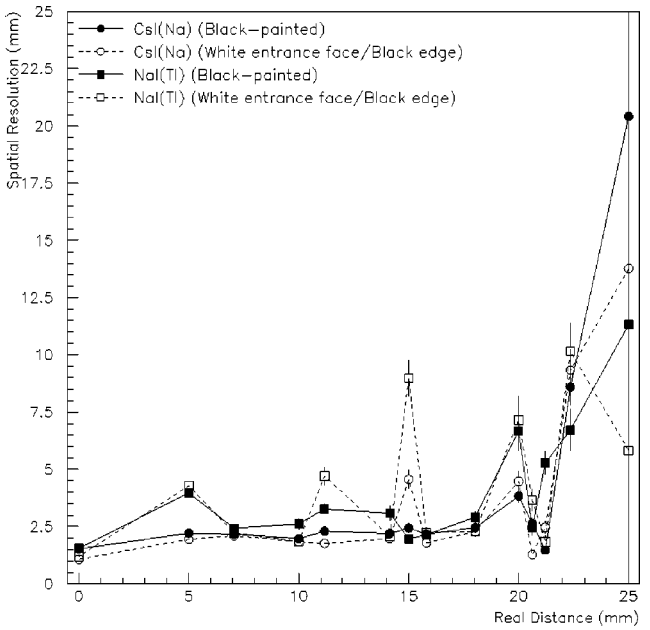

FIG. 10. Intrinsic spatial resolution values experimentally obtained as a function of the distance from the point considered to the center of the field of view.

tive discrepancies could be partially originated from the fact that PSPMT response inhomogeneity and compression effects have not been included in the simulations.

C. Energy resolution

Because of its very high luminescence efficiency, NaI(Tl) produces the highest signal per unit of absorbed radiation of the materials tested. In addition to this, the total light output in a white entrance face crystal due to light reflection on this surface, is greater than in a crystal with black painted entrance face. For that reason, the best energy resolutions ($\sim$15%) are obtained in the case of crystals with the entrance face white-painted/black edge, being slightly better for the NaI(Tl) crystal (Fig. 11). According to the laboratory test results obtained (imaging performance, spatial resolution, and energy resolution), we decided to use the CsI(Na)

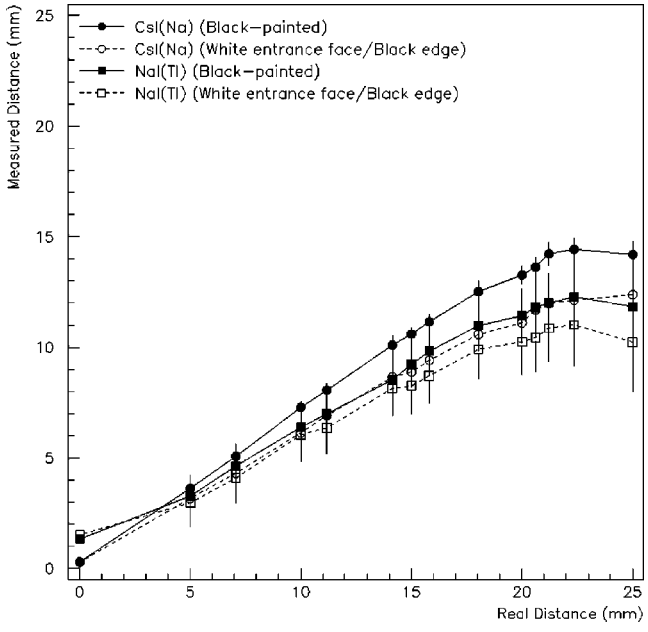

FIG. 9. Experimental intrinsic linearity curves obtained with CsI(Na) and NaI(Tl) crystals with two different surface finishes: black-painted and white-painted entrance face with black-painted edges. Real distance refers to the distance from the point considered to the center of the field of view.

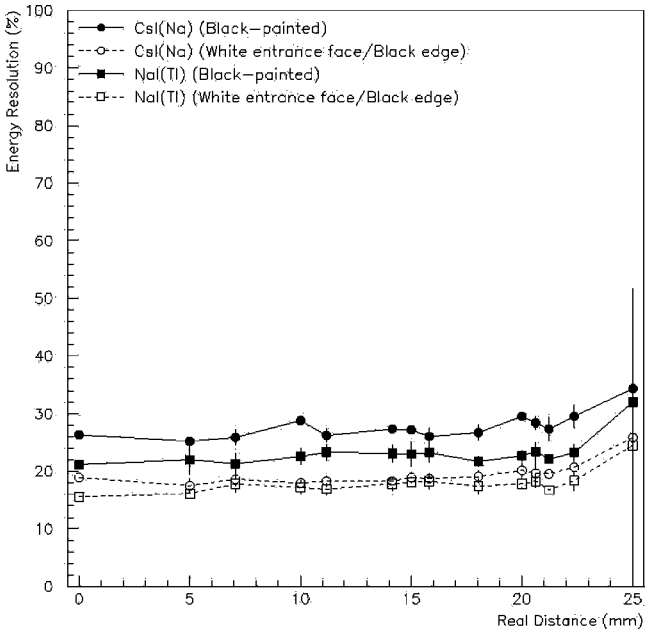

FIG. 11. Experimental intrinsic energy resolution as a function of the distance from the point considered to the center of the field of view for CsI(Na) and NaI(Tl) crystals with different surface treatments.

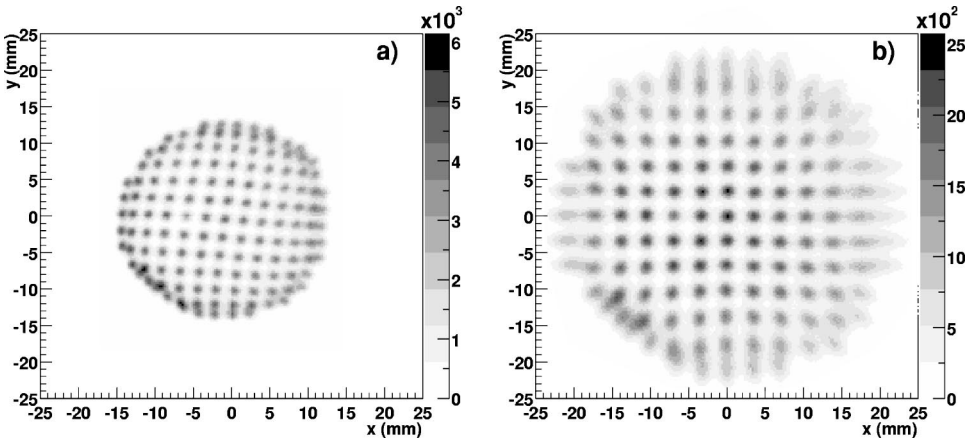

FIG. 12. (a) Image obtained with the lead calibration mask by direct application of Anger's equations. No spatial calibration of the signals has been done. (b) Corrected image after application of the reconstruction position procedure. Best fit is achieved for $M=8$ and $N=6$ [Eqs. (1) and (2)].

scintillator with black edges and white entrance face for our gamma camera. This configuration represents the best compromise between image compression, spatial resolution, and energy resolution among the configurations we have experimentally tested.

IV. CAMERA EVALUATION

The results discussed in the earlier section refer to intrinsic image features and energy resolution obtained without a camera collimator. The measurements were made under laboratory conditions, using collimated ^{57}Co (10 μCi, $E_\gamma = 122$ keV) point sources. The laboratory tests allowed us to decide /optimize the final configuration we will use in the gamma camera.

However, gamma camera calibration/performances must be obtained in real clinical conditions. These tests are described later.

A. Gamma camera calibration

Images shown in the previous section were obtained by direct application of Anger's equations to the PSPMT output signals. Due to the marked nonlinearity of the system, classical Anger's equations are not suitable for image formation due to the inhomogeneous compression that affects the image. Moreover, the lack of uniformity in gamma camera response (both in efficiency and pulse height) within the UFOV must be properly corrected in order to overcome as much as possible these inherent nonuniformities. Gamma camera calibration measurements were done at the Nou d'Octubre Hospital (Valencia, Spain), which provided us ^{99m}Tc source of the required activity. We placed on top of the gamma camera head a lead hole-mask 2 mm thick with 137 holes, 1 mm in diameter, covering the UFOV of the gamma camera. A non collimated 300 μCi ^{99m}Tc source, 2 mm in diameter, was placed at 23 cm from the head of the gamma camera in the center of the UFOV. This distance corresponds to about five times the UFOV.[21] The recorded image [Fig. 12(a)], had about 17×10^6 events in order to make sure that at least about 10^5 events cross each hole of the calibration mask. In order to obtain the corrected image, we have followed a polynomial functional fit to the data.[22] In this procedure we assume that our system can be approximated by two functions f and g, describing the system behavior along the X and Y axis, respectively. We know the values of those functions for a limited number of points (in our case such number is 137). We assume f and g to have a polynomial form

$$f(x_m,y_m)=\sum_{j=0}^{M} C_j\cdot x_m^{a_j}\cdot y_m^{b_j}, \tag{1}$$

$$g(x_m,y_m)=\sum_{j=0}^{N} D_j\cdot x_m^{c_j}\cdot y_m^{d_j}, \tag{2}$$

with

$$f(x_{mi},y_{mi})=x_{r_i}, \tag{3}$$

$$g(x_{mi},y_{mi})=y_{r_i} \qquad i=1...137, \tag{4}$$

(x_{ri},y_{ri}) being the "true" coordinate values and (x_{mi},y_{mi}) the measured coordinate values. The coefficients C_j, D_j, a_j, b_j, c_j, and d_j were fitted by least-square minimization using the ROOT package.[23] In a first step, we tried to fit the measured values by using one-dimensional dependence for f and g [i.e., $f=f(x_m)$, $g=g(y_m)$]. However such parametrization did not reproduce adequately the system behavior (reduced χ^2 of 5.5 while for the two-dimensional case we achieved a reduced χ^2 of 1.1). We also checked a two-dimension interpolation method,[24] but the results we obtained were slightly worse than those obtained with the two-dimensional polynomial fit. In Fig. 12(b) we show the corrected image after application of the position reconstruction procedure. Our procedure allow us to restore the image uniformity and linearity, specially at the edge region, as it will be discussed later (Secs. IV B 4 and IV B 5). Concerning the PSPMT pulse height nonuniformity, it has been corrected by renormalizing the value of the energy centroid at a given position to the value obtained for the central hole of the calibration mask.

Finally, energy calibration was done in the standard way by using four radioactive point sources: ^{57}Co($E_\gamma = 122.1$ keV), ^{241}Am($E_\gamma = 59.5$ keV), ^{133}Ba($E_\gamma = 81$ keV), and ^{99m}Tc($E_\gamma = 140.5$ keV).

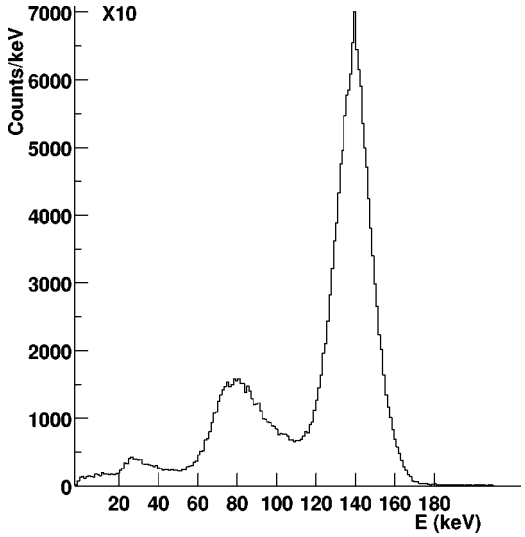

FIG. 13. Normalized ^{99m}Tc gamma camera energy spectrum. All the UFOV events have been considered.

B. Camera performances

Physical measurements according to the industry guidelines specified by the National Electrical Manufacturers Association (NEMA)[21] have been carried out in order to evaluate the camera performances. NEMA standards for gamma camera performance measurements have been established for large equipment, thus we had to adapt these guidelines to our system size and operating conditions. The sources used include a 2 mm diameter point source and a 2 mm capillary tube source, and two plastic petri dishes, 2.5 and 6 cm in diameter, for uniform flood sources. The test equipment included also a 2-mm-thick lead slit aperture with slits, 1 mm wide, separated by 5 mm. NEMA protocol requires to consider only events within a 20% energy window for the measurements described below and an event rate lower than 7000 counts/s for the selected window.

1. Energy resolution

For the gamma camera energy resolution measurement we placed on top of the gamma camera head the lead hole-mask 2 mm thick with 137 holes 1 mm in diameter covering the UFOV of the gamma camera we used previously for the gamma camera calibration (Sec. IV A). The non collimated ^{99m}Tc 2 mm in diameter source was placed at 23 cm from the head of the gamma camera in the center of the UFOV. NEMA specifications define the gamma camera energy resolution as the mean value of the full width half maximum (FWHM) (in percentage) for the energy distributions along the UFOV. In our case, the energy resolution varies between 11% at the center of the UFOV and 16% at the UFOV borders, being the mean value 13%, at the energy of interest (140 keV, see Fig. 13). It should be pointed out that the little discrepancy (about 4%) between the energy resolutions showed previously (Fig. 11) and those reported in this section is due to final electronic optimization carried out once the final configuration (scintillator and surface finish) were selected. Although most of the recently developed small gamma cameras are based on pixelated crystal arrays, this configuration often show FWHM energy resolution worse than 20% at around the 140 keV photopeak of ^{99m}Tc. However, Compton scattering can play an important role in the image background (in scintimammography, Compton scattering from the chest makes a major contribution to the background observed on the breast image).[25] Consequently a good energy resolution will considerably reduce Compton contribution and thus improve the quality of the recorded image. The energy resolution we obtain with our gamma camera allows to reduce Compton background on the image.

2. Spatial resolution

The intrinsic spatial resolution of the gamma camera was measured using the slit aperture placed on top of the gamma camera head. A 2 mm diameter ^{99m}Tc source was placed 23 cm away from the camera. According to NEMA specifications, measurements were done with the slits perpendicular to $X(Y)$ axis in order to obtain the intrinsic spatial resolution along $Y(X)$ axis. Final value for the intrinsic spatial resolution of the gamma camera is obtained as the mean value. NEMA standards indicate that gamma camera quality control specifications must be supplied also for the central field of view (CFOV), defined as the central 75% of the UFOV. Figure 14 shows the x- and y-direction line spread functions across the gamma camera field of view. The intrinsic spatial resolution of the system was 2.1 mm FWHM for the UFOV and 1.9 mm for the CFOV.

The system spatial resolution (i.e., gamma camera with collimator) was determined with and without scatter in the source following NEMA specifications. A 5-cm-thick plastic scattering block was located between the source and the camera for the measurements with scattering. For these measurements we used the 2 mm capillary tube source filled with a ^{99m}Tc solution. We evaluated the system resolution when equipped with three different collimators: a high resolution hexagonal parallel hole lead collimator (1.2 mm hole size, 0.2 mm septal thickness, and 35 mm length) and 2 lead pinhole collimators (2 and 3 mm in diameter, 4 mm thickness). For the pinhole collimators we chose a focal distance $f = 25$ mm. This is the minimum focal distance we can achieve with the current gamma camera design. Figure 15(a) shows the averaged (in the X and Y directions) system spatial resolution as a function of the source to collimator distance. In the case of pinhole collimators we show the resolution at the object plane. We have measured the system spatial resolution with scatter for a source to collimator distance of 35 mm. We have not found significant differences between the FWHM resolution measured with and without scatter in the case of pinhole collimators. As it can be expected, resolution deteriorates much more for the pinhole collimators than for the parallel hole collimator as the source to collimator distance increases. However, by increasing the source to collimator distance, the pinhole collimator configuration allows us to expand the UFOV at the object plane.

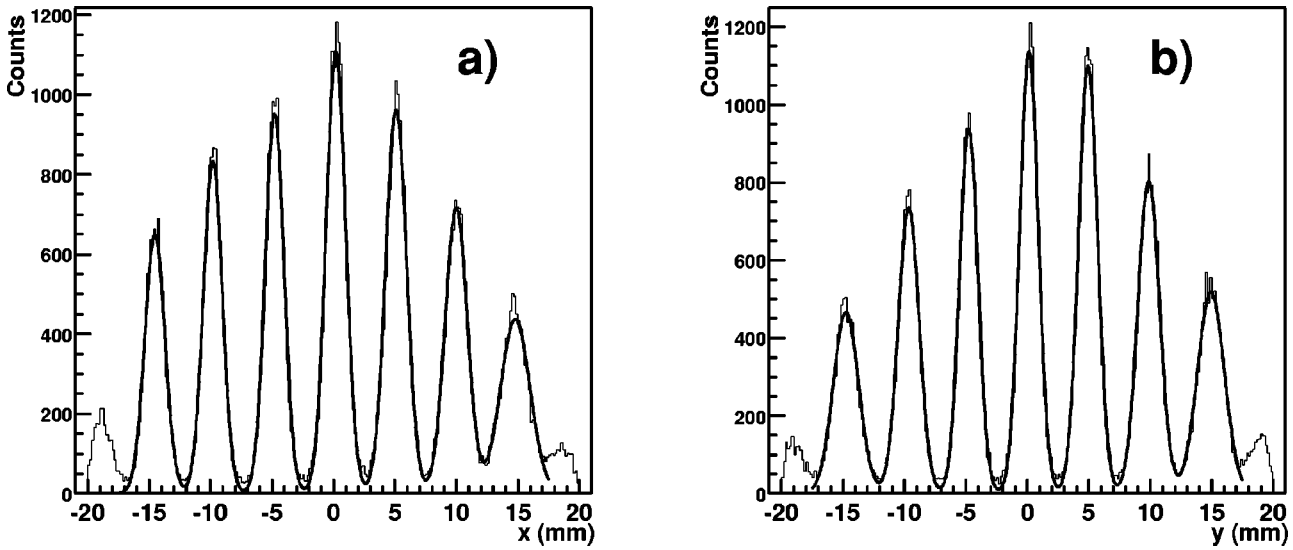

FIG. 14. (a) Line spread functions across the gamma camera field of view for the x direction. (b) Same as (a) for y direction.

3. Planar sensitivity

The planar sensitivity of our gamma camera was measured by placing a 25 mm diameter plastic petri dish filled to a depth of 1 mm with a ^{99m}Tc solution at the desired distance from the collimator surface. We determined the system planar sensitivity for the three collimators considered in this work. Figure 15(b) shows the gamma camera planar sensitivity as a function of the source to collimator distance. Only pinhole collimators values are displayed. For the parallel hole collimator we found a planar sensitivity value of 41 counts per minute per microCurie (cpm/μCi), independently of the source to collimator distance considered. For the 2 mm diameter lead pinhole collimator, planar sensitivity reaches up to 321 cpm/μCi for a source to collimator distance of 19 mm while for the 3 mm diameter pinhole we obtain 468 cpm/μCi at the same distance. However, it should be pointed out that a sensitivity increase factor ~ 2 should be expected when comparing 2 and 3 mm diameter pinhole instead of the observed 45% increase. This result can be explained if we consider the geometric tolerances, both in the diameter pinhole manufacturing and on the experimental setup. The difference of only 45% can be accounted for if we assume little deviations from the nominal values concerning pinhole diameter (i.e., pinhole diameter 2.1 instead of 2 mm and 2.9 instead of 3 mm) and setup geometry (1 mm error in the determination of the source-pinhole distance). Although sensitivity and spatial resolution for pinhole collimators significantly deteriorates as the source to collimator distance increases, this also increases the UFOV. This feature is quite important in our case, as we have only about 46 mm in diameter UFOV at the detector plane. For applications to small organs as thyroid and kidney scintigraphy as well as scintimammography, we should use a pinhole collimator in order to increase the UFOV at the object plane. Future gamma camera development will include also a diverging hole collimator to expand the UFOV,[15] which could have some advantages with respect to pinhole configuration.

4. Linearity

System linearity depends on the camera ability to properly identify the geometric coordinates of the interaction point for a given event. The geometric distortions can be determined by imaging the slit aperture in the same way as it was done for the intrinsic spatial resolution determination (Sec. IV B 2). We have followed NEMA specifications for the determination of the differential linearity and the absolute lin-

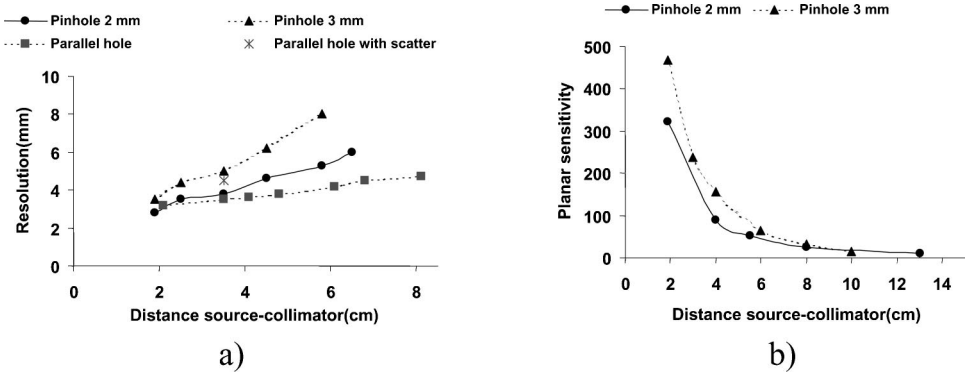

FIG. 15. (a) Extrinsic gamma camera resolution using three different collimators. We show also the resolution in the presence of scatter, when equipped with the parallel hole collimator. (b) Gamma camera planar sensitivity as a function of the source to collimator distance. Only pinhole collimator values are showed. Planar sensitivity is expressed in (cpm/μCi).

TABLE I. Physical characteristics of some recent reported small gamma cameras.

Reference	Crystal type	Crystal sizes (mm)	Field-of-view (cm^2)	Intrinsic spatial resolution (mm)	Energy resolution (%)
15	NaI(Tl)	Continuous, 6 mm thick	6×6	3.1	13
8	CsI(Tl)	2×2×3	10 cm diameter	1.6–1.8	17
3	CsI(Tl)	2×2×3	10 cm diameter	2	23 (@122 keV)
16	CsI(Na)	2×2×6	10×10	2.6	26
2, 26	NaI(Tl)	Continuous, 8 mm thick	7.3×7.3	1.7–2.8	15
5	CsI(Tl)	2.6×2.6×5	2.3×2.3	2.5	···
LumaGEM® HHGC[a]	···[b]	···[b]	1.25×1.25	1.0–1.25	···
γ IMAGER[c]	CsI(Na)	Continuous, 4 mm thick	10 cm diameter	2	11
IMI Gamma Camera[d]	···	···	5.5 cm diameter	3.5	···
This work	CsI(Na)	Continuous, 4 mm thick	5 cm diameter	1.9–2.1	13

[a]Gamma Medica™, Inc., http://www.intra-medical.com.
[b]LumaGEM Hand Held Gamma Camera may employ different scintillation arrays with crystals of various sizes.
[c]Biospace Mesures, Paris, http://www.biospace.fr.
[d]IntraMedical Imaging, Inc., http://www.intra-medical.com/IMI/mcam.html.

earity. The differential linearity is defined as the standard deviation between the measured coordinates and those of the best fit to a straight line through these measured positions.[21] The differential linearity must be specified as the mean value for the *X* and *Y* directions and for the UFOV and the CFOV. We obtain a system differential linearity of 0.17 mm for the UFOV and 0.15 mm for the CFOV, with no significant differences between the *X* and *Y* directions. The absolute linearity can be defined as the maximum deviation between the measured coordinates with respect to the real position coordinates. Maximum deviation refers to that obtained separately for the *X* and *Y* directions. Again, absolute linearity must be specified for the UFOV and the CFOV. For the UFOV we obtain an absolute linearity of 0.87 and 0.28 mm for the CFOV. Both values were obtained at the *X* direction, while the maximum deviation at the *Y* direction was 0.56 and 0.16 mm for the UFOV and the CFOV, respectively. As a consequence of the calibration process (Sec. IV A) we overcome the marked nonlinear behavior of the camera, mainly originated by the use of a continuous scintillation crystal and no additional image linearization procedure is needed.

5. Spatial uniformity

In normal operation conditions, images recorded with gamma cameras must be corrected for spatially dependent nonuniformity in the camera sensitivity. This correction is performed by dividing a uniform flood image in a pixel-by-pixel basis and renormalizing to an averaged pixel value. We have followed NEMA protocol for the determination of the integral and the differential uniformity. The integral uniformity is defined as the difference between the maximum and minimum pixel counts, for a uniform flood image, divided by their sum. The differential uniformity is defined similarly, but measures the maximum difference in counts between pixels separated by a distance of no more than five pixels along either a row or a column. The integral and differential uniformity must be specified for the UFOV and the CFOV. The flood field image was obtained by using a 6 cm diameter plastic petri dish filled with a ^{99m}Tc solution. The gamma camera was equipped with the parallel hole collimator.

We obtained a system differential uniformity of 8.1% in both, the UFOV and the CFOV. Concerning integral uniformity, we obtain for the UFOV a value of 14.1% and 4.7% for the CFOV. Our calibration process (Sec. IV A) allow us to obtain a remarkable image uniformity and no additional image treatment is needed. These values should be compared with those reported in the literature for small field of view gamma cameras.

Values of 25%,[16] 29%,[2,26] and 18%[3] have been reported for the UFOV integral uniformity, while 23%[2,16,26] and 13.5%[3] values were obtained for the differential uniformity. We can state that our gamma camera shows a quite good uniformity behavior when compared with other small gamma cameras recently developed.

6. Comparison with other small gamma cameras

Table I compares the main features of our gamma camera with other small gamma cameras recently reported in the literature together with some commercialized at present by different entities. It is interesting to point out that our camera shows an intrinsic spatial resolution similar to that obtained with much more complex crystal array based gamma cameras. Finally, we would like to emphasize that our camera is fully portable, and no external electronic devices are required as the camera is only connected through the USB port to a portable PC. No acquisition card must be installed on the PC. These features represent an important advantage with respect to other small gamma cameras, some of them using CAMAC and NIM external electronic modules.

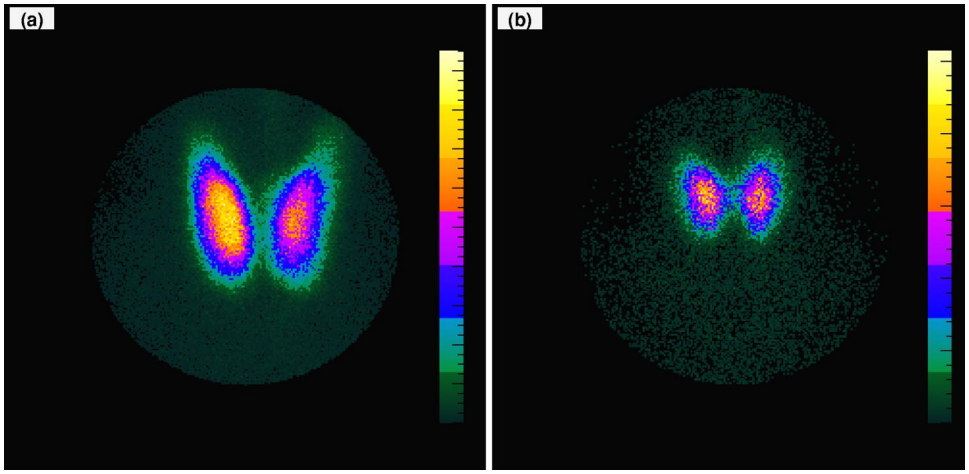

FIG. 16. Thyroid images acquired with the minigamma camera and the 2 mm diameter pinhole collimator. Both cases correspond to hyperthyroidism. (a) 740 s acquisition time with a counting rate of 510 counts/s. (b) 170 s acquisition time with a counting rate of 300 counts/s.

V. CLINICAL TEST

In order to determine the gamma camera capabilities we evaluated its performances at the Nuclear Medicine Service of the Nou d'Octubre Hospital (Valencia, Spain). In accordance with the requirements of the local ethical committee, informed consent from the patients was obtained prior to the examination. For this clinical evaluation, we compared thyroid images acquired with our camera with those obtained with the general purpose gamma camera of the hospital (APEX SP-4HR model manufactured by Elscint, 46 cm FOV equipped with 61 PMTs). Considering the normal sizes for the adult's thyroid and our detector FOV, we do not considered the parallel hole collimator for these measurements. The general purpose gamma camera was equipped wit a 4 mm in diameter pinhole collimator, with a focal distance $f = 11$ cm. Considering pinhole collimator diameter aperture of the general purpose gamma camera, we compared directly measurements done with our camera equipped with the 3 mm diameter pinhole collimator. The ^{99m}Tc injected dose to the patients was 6 mCi, and the acquisition with the general purpose gamma camera started 25 min after the administration. The measurement with our camera started about 40 min after the general purpose gamma camera image acquisition. In Fig. 16 we show two images recorded with our gamma camera with the 2 mm diameter pinhole collimator corresponding to two hyperthyroidism cases. Only events within the 20% energy window were considered. The acquisition times were 740 and 170 s, with counting rates of 510 and 300 counts per second, for cases (a) and (b) in Fig. 16, respectively. In Fig. 17, we show two thyroid clinical cases (hyperthyroidism and a thyroid nodule) imaged with our minigamma camera with the 3 mm diameter pinhole collimator while in Fig. 18 we show the same cases imaged with the general purpose gamma camera. As usually, only events within the 20% energy window were considered. The acquisition times with the small gamma camera were comparable with those of the general purpose gamma camera. However, the counting rate for the small gamma camera was about 60% of that obtained with the general purpose gamma camera. This difference could be explained if we consider the different areas subtended by the pinhole collimators used in both cameras. Moreover, as it was already pointed out, the measurement with our camera started about 40 min after the general purpose gamma camera image acquisition. Although this delay time represents only about 5% ^{99m}Tc activity difference between both measurements, the ^{99m}Tc biodistribution could change during this interval time, decreasing the radionuclide concentration on the thyroid. Nevertheless,

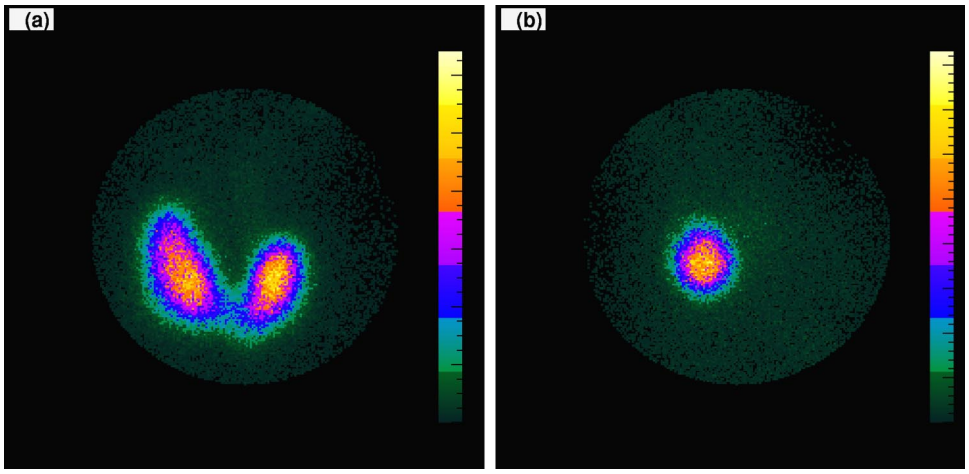

FIG. 17. Thyroid images acquired with the minigamma camera and the 3 mm diameter pinhole collimator. The (a) case corresponds to hyperthyroidism, while (b) corresponds to a thyroid nodule. The acquisition times were 280 and 250 s for the cases (a) and (b), respectively.

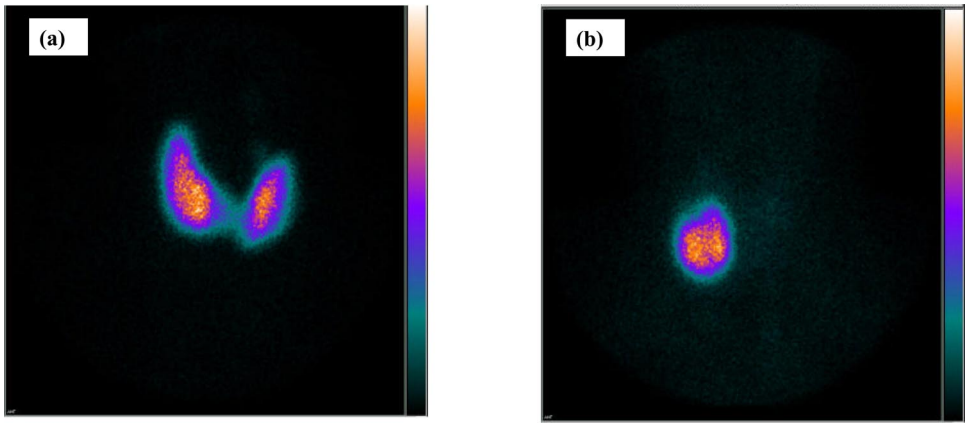

FIG. 18. Same cases as in Fig. 17 but recorded with the general purpose gamma camera. The acquisition times were 160 and 380 s for the cases (a) and (b), respectively.

there is not a significant loss of image quality if we compare the images obtained with our small gamma camera and that obtained with the general purpose gamma camera. It is also interesting to point out that despite the lower energy resolution of our camera when compared with standard gamma cameras, the camera works adequately in realistic conditions. By comparing 2 and 3 mm diameter pinhole images (Figs. 16 and 17) we do not observe any significant degradation of the image when the 3 mm pinhole is used. For that reason we believe that the 3 mm pinhole collimator could be more suitable for thyroid imaging, due to its higher sensitivity. In any case, our gamma camera mechanical design allows the collimators (both pinhole and parallel hole) used in this work to be quickly and easily interchanged. Although the clinical validation of the small gamma camera described in this work has just started, these preliminary results indicate that we can achieve comparable results to that obtained with more complex, and thus costly, small field of view gamma cameras developed until now.

VI. CONCLUSIONS

A small, fully portable, and low cost gamma camera for medical applications has been designed, built, and tested, both at laboratory and clinical levels. This gamma camera provides image quality comparable to that obtained with more complex, and thus costly, small field of view gamma cameras developed until now.

The minigamma camera has an overall size of 90 mm diameter and 200 mm length with a total weight of 2 kg. Special emphasis has been put on low cost and high portability. All the electronic components, including the ADC and the PSPMT power supply, are packed inside the minigamma camera and no external electronic devices are required. The camera is only connected through the USB port to a portable PC, and no acquisition card must be plugged into the PC. We have developed a specific data processing software which allows to control both the camera parameters, including PSPMT high voltage power supply, and the measuring process. The software also displays on the PC the acquired image in real time. This camera, optimised for ^{99m}Tc, is based on a Hamamatsu R2486 position-sensitive photomultiplier tube and a continuous CsI(Na) $51\times51\times4$ mm scintillation crystal. Simulations and experimental tests were carried out in order to characterize and optimize its main components, such as the position-sensitive photomultiplier and the scintillation detector. After camera calibration was performed for the correction of the nonlinearity and nonuniformity in the gamma camera response, the camera performances have been measured following NEMA standards, providing intrinsic spatial resolution of about 2 mm and an energy resolution of 13% at 140 keV within the UFOV of 46 mm. We evaluated the gamma camera capabilities when equipped with three different collimators: a parallel hole and two pinhole lead collimators. For applications to small organs such as thyroid and kidney scintigraphy as well as for scintimammography, we should use pinhole collimators to increase the UFOV at the object plane. The minigamma camera described in this work shows good linearity position and uniformity response when compared with other small gamma cameras recently developed. Finally, the minigamma camera was clinically evaluated, and thyroid images acquired with our camera were compared with those obtained with a general purpose gamma camera without a significant loss in image quality.

ACKNOWLEDGMENTS

The authors acknowledge the help and collaboration of Dr. R. Sopena and Dr. D. López from the Nou d'Octubre Hospital of Valencia. This work was supported by European Community funds under Grant No. 1FD97-2387.

[a]Author to whom correspondence should be addressed. Electronic mail: filomeno@ific.uv.es

[1] H. O. Anger, "Scintillation camera," Rev. Sci. Instrum. **29**, 27–33 (1958).
[2] K. L. Matthews, "Development and application of a small gamma camera," Med. Phys. **24**, 1802 (1997).
[3] C. L. Maini, F. de Notaristefani, A. Tofani, F. Iacopi, R. Sciuto, A. Semprebene, T. Malatesta, F. Vittori, F. Frezza, C. Botti, S. Giunta, and P. G. Natali, "99-m-Tc-MIBI scintimammography using a dedicated nuclear mammograph," J. Nucl. Med. **40**, 46–51 (1999).
[4] R. Pani, R. Pellegrini, F. Scopinaro, A. Soluri, G. De Vincentis, A. Pergola, F. Iacopi, A. Corona, A. Grammatico, S. Filippi, and P. L. Ballesio, "Scintillating array gamma camera for clinical use," Nucl. Instrum. Methods Phys. Res. A **392**, 295–298 (1997).
[5] A. Soluri, R. Scafè, F. Capoccetti, N. Burgio, A. Schiaratura, R. Pani, R. Pellegrini, M. N. Cinti, M. Mechella, A. Amanti, V. David, and F.

Scopinaro, ''Imaging probe for breast cancer localization,'' Nucl. Instrum. Methods Phys. Res. A **497**, 114–121 (2003).
[6] F. Garibaldi, E. Cisbani, S. Colilli, F. Cusanno, F. Giuliani, M. Gricia, M. Lucentini, L. Pierangeli, F. Santavenere, G. M. Urciuoli, R. Pani, R. Pellegrini, M. N. Cinti, and R. Scafe, ''Scintillator and photodetector array optimization for functional breast imaging,'' Nucl. Instrum. Methods Phys. Res. A **497**, 51–59 (2003).
[7] E. Itti, B. E. Patt, L. E. Diggles, L. MacDonald, J. S. Iwanczyk, F. S. Mishkin, and I. Khalkhali, ''Improved scintimammography using a high-resolution camera mounted on an upright mammography gantry,'' Nucl. Instrum. Methods Phys. Res. A **497**, 1–8 (2003).
[8] F. Scopinaro, R. Pani, G. De Vincentis, A. Soluri, R. Pellegrini, and L. M. Porfiri, ''High-resolution scintimammography improves the accuracy of technetium-99m methoxyisobutylisonitrile scintimammography: Use of a new dedicated gamma camera,'' Eur. J. Nucl. Med. **26**, 1279–1288 (1999).
[9] F. Scorpinaro and R. Massa, ''Role and perspectives of scintimammography,'' Nucl. Instrum. Methods Phys. Res. A **497**, 14–20 (2003).
[10] E. J. Hoffman, M. P. Tornai, C. S. Levin, L. R. MacDonald, and S. Siegel, ''Gamma and beta intraoperative imaging probes,'' Nucl. Instrum. Methods Phys. Res. A **392**, 324–329 (1997).
[11] D. J. Wagenaar, S. Chowdhury, J. C. Engdahl, and D. D. Burckhardt, ''Planar image quality comparison between a CdZnTe prototype and a standard NaI(Tl) gamma camera,'' Nucl. Instrum. Methods Phys. Res. A **505**, 586–589 (2003).
[12] C. Scheiber and G. C. Giakos, ''Medical applications of CdTe and CdZnTe detectors,'' Nucl. Instrum. Methods Phys. Res. A **458**, 12–25 (2001).
[13] C. S. Levin, ''Detector design issues for compact nuclear emission cameras dedicated to breast imaging,'' Nucl. Instrum. Methods Phys. Res. A **497**, 60–74 (2003).
[14] C. L. Menard, Y. Charon, M. Solal, M. Ricard, P. Lanièce, R. Mastrippolito, L. Pinot, and L. Valentin, ''Performance characterization and first clinical evaluation of a intraoperative compact gamma imager,'' IEEE Trans. Nucl. Sci. **46**, 2068–2074 (1999).
[15] J. Kim, Y. Choi, K. Joo, B. Sihn, J. Chong, S. E. Kim, K. H. Lee, Y. S. Choe, and B. Kim, ''Development of a miniature scintillation camera using an NaI(Tl) scintillator and PSPMT for scintimammography,'' Phys. Med. Biol. **45**, 3481–3488 (2000).
[16] M. B. Williams, A. R. Goode, V. Galbis-Reig, S. Majewski, A. G. Weisenberger, and R. Wojcik, ''Performance of a PSPMT based detector for scintimammography,'' Phys. Med. Biol. **45**, 781–800 (2000).
[17] N. D. Giokaris, G. K. Loudosb, D. Maintase, D. Papapanagiotoue, K. S. Nikitab, N. K. Uzunoglub, A. Karabarbounisa, C. N. Papanicolasa, E. Stiliarisa, S. C. Archimandritisd, A. D. Varvarigoud, C. N. Stefanisf, S. Majewskig, A. Weisen-bergerg, R. Panih, and F. Scopinaro, ''Imaging of breast phantoms using a high-resolution position sensitive photomultiplier tube,'' Nucl. Instrum. Methods Phys. Res. A **497**, 141–149 (2003).
[18] C. E. Ordoñez, R. A. Mintzer, S. N. Aarsvold, N. J. Yasillo, and K. L. Matthews, ''Simulation of imaging with sodium iodide crystals and position-sensitive photomultiplier tubes,'' IEEE Trans. Nucl. Sci. **41**, 1510–1515 (1994).
[19] N. Pavón, ''Design development and test of the analog and digital electronics for a portable gamma camera,'' Advanced Studies Degree, University of Valencia, Spain, 2002.
[20] A. J. Bird, ''A position sensitive detector for hard x-ray astronomy,'' Ph.D. thesis, University of Southampton, England, 1990.
[21] ''Performance measurements of scintillation cameras,'' *NEMA Standards Publication No. NU 1* (National Electrical Manufacturers Association, Washington, DC, 1994).
[22] B. Carnahan, H. A. Luther, and J. O. Wilkes, *Applied Numerical Methods* (Wiley, New York, 1969).
[23] R. Brun, ''ROOT: An object-oriented data analysis framework,'' CERN Data Handling Division, 2001.
[24] W. H. Press, S. A. Teukolsky, B. P. Flannery, and W. T. Vetterling, *Numerical Recipes. The Art of Scientific Computing* (Cambridge University Press, Cambridge, 1989).
[25] R. Pani, F. Scopinaro, R. Pellegrini, A. Soluri, I. N. Weinberg, and G. De Vincentis, ''The role of Compton background and breast compression on cancer detection in scintimammography,'' Anticancer Res. **17**, 1645–1649 (1997).
[26] K. L. Mattews, ''Development and application of a small gamma camera,'' Ph.D. thesis, University of Chicago, 1997.